

Meshfree Collocation for Elliptic Problems with Discontinuous Coefficients

Heinrich Kraus^{a,b,*}, Jörg Kuhnert^a, Andreas Meister^b, Pratik Suchde^{a,c}

^a*Fraunhofer ITWM, Fraunhofer-Platz 1, 67663 Kaiserslautern, Germany*

^b*Universität Kassel, Heinrich-Plett-Straße 40, 34132 Kassel, Germany*

^c*University of Luxembourg, 2 Av. de l'Université, 4365 Esch-sur-Alzette, Luxembourg*

Abstract

We present a meshfree generalized finite difference method (GFDM) for solving Poisson's equation with coefficients containing jump discontinuities up to several orders of magnitude. To discretize the diffusion operator, we formulate a strong form method that uses a smearing of the discontinuity, and a conservative formulation based on locally computed Voronoi cells. Additionally, we propose a novel conservative formulation of enforcing Neumann boundary conditions that is compatible with the conservative formulation of the diffusion operator. Finally, we introduce a way to switch between the strong form and the conservative formulation to obtain a locally conservative and positivity preserving scheme. The presented numerical methods are benchmarked against four test cases with varying complexity and different jump magnitudes on point clouds that are not aligned to the discontinuity. Our results show that the new hybrid method that switches between the two formulations produces better results than the standard GFDM approach for high jumps in the diffusivity parameter.

Keywords: Anisotropic Laplacian, Discontinuous Coefficients, Meshfree, Collocation, GFDM

1. Introduction

The present work lays the foundation of simulations of phase change processes with a meshfree generalized finite difference method (GFDM) [1, 2, 3]. The eventual goal is to describe a multiphase flow in a monolithic approach without explicitly distinguishing between the different phases or tracking the interfaces. This approach leads to jumps in material coefficients, such as thermal conductivity, density and viscosity [4]. All of these material properties appear in diffusion operators of the form $\nabla \cdot (\eta \nabla u)$ with discontinuities in η . This is the reason to study Poisson's equation in divergence form in more detail.

There exists a number of approaches on approximating the diffusion operator with jumping coefficients and simulation of phase change processes. For problems where the interface is

*Corresponding author: heinrich.kraus@itwm.fraunhofer.de

known, such as compound materials, a common approach is a domain decomposition where the two materials are treated as separate subdomains with interface conditions connecting them [5, 6]. Since in our future applications, we have no knowledge of the position of the interface, we would need to compute a domain decomposition based on physical properties such as the temperature. However, this is computationally heavy and unfeasible in practical applications where a domain decomposition has to be computed once or even multiple times per time step. Another common approach is given by the class of level-set methods [7]. There the interface is given by a level-set function that serves as an identifier to which phase a point in the computational domain belongs. This can also be used for smeared-out or diffuse interfaces, but level-set methods require us to solve for an additional function, the level-set function. This also means that we need to set an initial level-set function. However, it is often desirable for the interface between the two phases to emerge naturally without the need to specify a time and location of its emergence. An alternative approach is the use of enrichment which has been used in meshfree methods [8, 9] and finite element methods [10, 11, 12] alike. The goal there is to extend the basis of the function space, usually by discontinuous functions, and to achieve more accurate results that way. In present literature that deals with strong-form methods, the jumps are only of a few orders of magnitude [13, 14, 15]. The jumps in phase change simulations can be of several orders of magnitude such that existing methods are generally not used for these applications.

Our eventual motivation, beyond the scope of the present work, is to use a meshfree GFDM in a Lagrangian framework [16, 17] for phase change processes. The method approximates strong form differential operators that are computed on local neighborhoods. However, it fails to ensure flux conservation in its core formulation which can lead to numerical instabilities. Several approaches have been pursued to eradicate this issue but only offer partial solutions. Suchde et al. [18] provide a weaker notion of flux conservation. Other approaches have been presented [19, 15] to establishing differential operators globally that violate the local nature of differential operators and thus are too expensive to be used for time-varying point clouds.

In this paper, we introduce a method that does not depend on any a priori knowledge of the interface. It strives to identify the interface based on algebraic properties from the strong formulation of the diffusion operator calculation, and switches over to a conservative method that is based on locally computed control volumes. In the finite volume method, such control volumes are based on a globally defined mesh. In contrast, the control volumes here are computed locally [18].

This paper is organized as follows. In section 2, we formulate Poisson’s equation in divergence form and give a brief introduction in the generalized finite difference method. After that, we establish properties that our numerical methods have to fulfill and develop the strong form weighted-least-squares and the conservative control volume based discretization of the diffusion operator. Finally, we introduce a way of combining these approaches into a hybrid formulation. These methods are benchmarked in section 3 against four test cases with varying complexity. We conclude the paper with a brief discussion of the methods and numerical results in section 4 and a conclusion in section 5.

2. Method Formulation

We consider Poisson's equation

$$-\nabla \cdot (\eta \nabla u) = f \quad (1)$$

on a domain $\Omega \subset \mathbb{R}^d$ with a diffusivity parameter $\eta = \eta(\mathbf{x}) > 0$. Additionally, we set Dirichlet and Neumann boundary conditions

$$u|_{\partial\Omega_D} = g_D \quad (2a)$$

$$\left. \frac{\partial u}{\partial \mathbf{n}} \right|_{\partial\Omega_N} = g_N \quad (2b)$$

with a disjoint partition of the boundary $\partial\Omega$ into $\partial\Omega_D$ and $\partial\Omega_N$. We also use the abbreviatory notation

$$Lu := \nabla \cdot (\eta \nabla u). \quad (3)$$

In our case, we are interested in diffusivity parameters η that have one or multiple jumps, possibly of several orders of magnitude. This represents jumps in material properties that can occur during a phase change process or a multiphase problem.

We generally assume that a unique solution $u \in H^1(\Omega)$ exists, see for example [20] where a general theory is presented. Because of that, we are interested in solutions that satisfy the jump conditions

$$[[u]] = 0 \quad (4a)$$

$$[[\eta \nabla u]] = \mathbf{0}. \quad (4b)$$

2.1. Generalized Finite Difference Method

In our GFDM, we use a point cloud for the spatial discretization. A point cloud associated to Ω consists of a finite set of points

$$\Omega_h = \{\mathbf{x}_1, \dots, \mathbf{x}_N\} \subset \bar{\Omega} = \Omega \cup \partial\Omega$$

together with an interaction radius $h: \Omega \rightarrow \mathbb{R}$. For an arbitrary function $u: \Omega \rightarrow \mathbb{R}$ we write $u_i = u(\mathbf{x}_i)$ and $\mathbf{u} = (u_1, \dots, u_N)^T$. The interaction radius is also sometimes called smoothing length and induces a distance function $d: \Omega \times \Omega \rightarrow [0, \infty)$ that measures the relative distance between points in our point cloud. For example, we can use a scaled Euclidean distance

$$d_1(\mathbf{x}_j, \mathbf{x}_i) = \frac{\|\mathbf{x}_j - \mathbf{x}_i\|}{h_i}$$

or

$$d_2(\mathbf{x}_j, \mathbf{x}_i) = \frac{2\|\mathbf{x}_j - \mathbf{x}_i\|}{h_j + h_i}.$$

With this, we can define neighborhoods

$$B_i = \{ \mathbf{x}_j \in \Omega_h \mid d(\mathbf{x}_j, \mathbf{x}_i) \leq 1 \} \quad (5)$$

and their respective index sets

$$S_i = \{ j \mid \mathbf{x}_j \in B_i \} \quad (6)$$

for each point \mathbf{x}_i . We call neighborhoods symmetric if

$$j \in S_i \implies i \in S_j$$

is satisfied for each point. This can be guaranteed only when the distance function used is symmetric. Hence, by using d_1 we obtain radial but not necessarily symmetric neighborhoods and d_2 leads to symmetric but not necessarily radial neighborhoods. Neighborhoods are used to establish a notion of connectivity between points, based on which numerical computations can be executed.

In the strong form GFDM [21, 22, 23, 24, 25], for a linear differential operator D^* , we seek a numerical representation D_i^* of that differential operator at point \mathbf{x}_i given by coefficients c_{ij}^* such that

$$D^*u(\mathbf{x}_i) \approx D_i^*u = \sum_{j \in S_i} c_{ij}^* u_j.$$

Here the asterisk is a placeholder for any differential operator, such as the Laplacian Δ or the partial derivative ∂_{x_k} with respect to variable x_k . To compute the coefficients c_{ij} , we impose exact reproducibility of monomial test functions

$$D^*(\mathbf{x} - \mathbf{x}_i)^\alpha = \sum_{j \in S_i} c_{ij}^* (\mathbf{x}_j - \mathbf{x}_i)^\alpha \quad (7)$$

for all multi-indices $\alpha \in \mathbb{N}_0^d$ with $|\alpha| \leq K$. Here, the usual notations $\mathbf{x}^\alpha = \prod_{n=1}^d x_n^{\alpha_n}$ and $|\alpha| = \sum_{n=1}^d \alpha_n$ are used. This leads to fewer conditions than the number points in the neighborhood which results in an under-determined linear system. We thus add a minimization constraint

$$\min \sum_{j \in S_i} \left(\frac{c_{ij}^*}{w_{ij}} \right)^2 \quad (8)$$

on the coefficients. The weights $w_{ij} > 0$ are chosen as

$$w_{ij} = \exp \left(-\alpha \frac{\|\mathbf{x}_j - \mathbf{x}_i\|}{h_i + h_j} \right) \quad (9)$$

with a weighting factor $\alpha > 0$. We combine equations (7) and (8) into an optimization problem in matrix form

$$\min \|\mathbf{W}_i^{-1} \mathbf{c}_i^*\| \quad (10a)$$

$$\text{s.t. } \mathbf{K}_i \mathbf{c}_i^* = \mathbf{b}_i^* \quad (10b)$$

with the solution given as [23, 18]

$$\mathbf{c}_i^* = \mathbf{W}_i^2 \mathbf{K}_i^T (\mathbf{K}_i \mathbf{W}_i^2 \mathbf{K}_i^T)^{-1} \mathbf{b}_i^*. \quad (10c)$$

Here the weights w_{ij} are written in a $|S_i| \times |S_i|$ diagonal matrix \mathbf{W}_i . Each row of matrix \mathbf{K}_i represents one test function applied to the points in the neighborhood and \mathbf{b}_i^* are the exact evaluations of the differential operators to the respective monomial test function.

2.2. Discretization of the Diffusion Operator

For our Poisson's equation (1), we seek coefficients γ_{ij} such that we obtain an approximation to the diffusion operator (3)

$$Lu(\mathbf{x}_i) \approx L_i u = \sum_{j \in S_i} \gamma_{ij} u_j. \quad (11)$$

The coefficients γ_{ij} form a matrix \mathbf{G} to obtain the discrete Poisson's equation

$$\mathbf{G} \mathbf{u} = \mathbf{f} \quad (12)$$

together with the boundary conditions. From the theory on elliptic and parabolic operators, see for example Chipot [20], it is known that the maximum principle

$$-Lu \geq 0 \implies u \geq 0 \quad (13)$$

holds even for low regularity of the diffusivity η and the source term f . This property is usually carried over to numerical schemes as well [26]. However, GFDM in its current strong form approach has no means to guarantee the discrete maximum principle

$$\mathbf{f} \geq \mathbf{0} \implies \mathbf{u} \geq \mathbf{0} \quad (14)$$

without solving a global linear system [23].

The lack of a discrete maximum principle arises not only in GFDM but also in many other meshfree collocation approaches. To guarantee the maximum principle discretely, one way is for our system matrix \mathbf{G} to be an M-matrix. A broad theory on M-matrices for GFDM is presented by Seibold [27]. The results needed in our application can be briefly summarized by a sign condition $\gamma_{ii} < 0$ and the diagonal dominance criterion

$$\sum_{\substack{j \in S_i \\ j \neq i}} |\gamma_{ij}| \leq |\gamma_{ii}|$$

for the coefficients in equation (11).

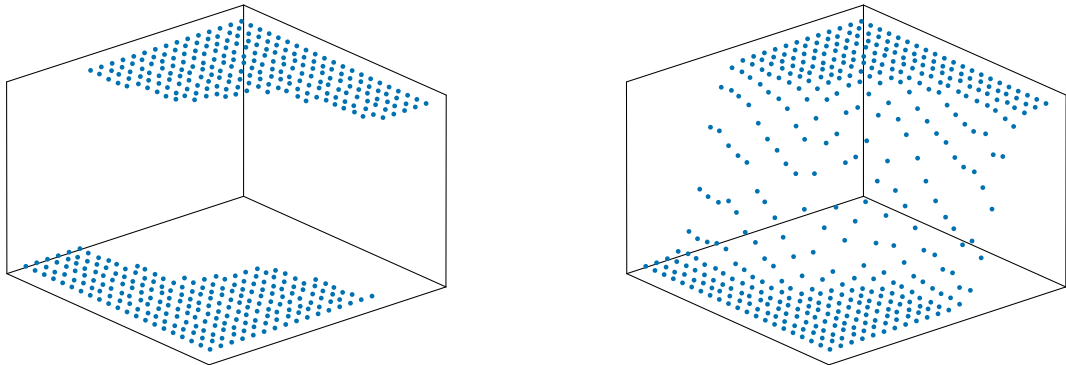


Figure 1: Comparison of discontinuous function (left) and its smoothed counterpart (right) with 2 smoothing cycles.

2.2.1. Classical Operator

For the strong form GFDM, we assume that the diffusivity parameter η is sufficiently smooth. This is of course not the case for a discontinuous diffusivity parameter. To overcome this, we smooth η using weights $w_{ij} \geq 0$ in a convex combination of function values over the neighborhood

$$\tilde{\eta}_i = \frac{\sum_{j \in \mathcal{S}_i} w_{ij} \eta_j}{\sum_{j \in \mathcal{S}_i} w_{ij}}.$$

In our case, the weights are similar to those in equation (9). However, they need not be the same. The smoothing process can be applied multiple times, leading to an incrementally increasing smearing of the jump. In figure 1, a discontinuous function with its smoothed equivalent is depicted. Let $\tilde{\eta}$ be the smoothed diffusivity, then we can apply rules for differentiation on the diffusion operator (3) to obtain

$$Lu \approx \nabla \cdot (\tilde{\eta} \nabla u) = \nabla \tilde{\eta} \nabla u + \tilde{\eta} \Delta u. \quad (15)$$

Alternatively, it is sometimes advantageous to use the scaled diffusivity parameter $\mu = \log \eta$, especially when there are large jumps in η . This yields, after potential smoothing steps, the diffusion operator

$$Lu = \nabla \cdot (\exp(\mu) \nabla u) \approx \nabla \cdot (\exp(\tilde{\mu}) \nabla u) = \exp(\tilde{\mu}) (\nabla \tilde{\mu} \nabla u + \Delta u). \quad (16)$$

In both cases we have to compute the gradient of either $\tilde{\eta}$ or $\tilde{\mu}$ if we want to use monomial test functions of degree 1 or higher. Since the gradient is not known, we have to compute it numerically. This can be a source of inaccuracy since we not only numerically compute the gradient but also use a smoothed and thus distorted diffusivity coefficient. The coefficients γ_{ij} are then computed by solving the optimization problem (10).

Since the optimization problem (10) does not impose a condition of diagonal dominance, this can lead to non-diagonally dominant rows and in some cases instabilities in the numerical

solution [23]. To reduce numerical instabilities, a correction technique has been developed where a correction vector $\boldsymbol{\xi}_i$ is computed that lies in the null space of the test function space

$$\sum_{j \in S_i} \xi_{ij} (\mathbf{x}_j - \mathbf{x}_i)^\alpha = 0$$

for all monomials being considered. To obtain a non-trivial zero operator $Z(m) = 0$ on the space of monomial test functions, an additional constraint $\xi_{ii} = 1$ is added. With this, we can define a new operator

$$\mathbf{a}_i = \boldsymbol{\gamma}_i + \alpha \boldsymbol{\xi}_i \quad (17)$$

that satisfies the constraints from the optimization problem (10b). In the next step, we minimize the function

$$\phi(\alpha) = \sum_{j \in S_i} \frac{(c_{ij}^* + \alpha \xi_{ij})^2}{(c_{ii}^* + \alpha \xi_{ii})^2}$$

which leads to [23]

$$\alpha = \frac{c_{ii}^* \langle \mathbf{c}_i^*, \boldsymbol{\xi}_i \rangle - \xi_{ii} \langle \mathbf{c}_i^*, \mathbf{c}_i^* \rangle}{\xi_{ii} \langle \mathbf{c}_i^*, \boldsymbol{\xi}_i \rangle - c_{ii}^* \langle \boldsymbol{\xi}_i, \boldsymbol{\xi}_i \rangle}.$$

This correction does not guarantee diagonally dominant operators and there are numerous examples of neighborhoods where this technique does not provide diagonally dominant rows. This can be observed especially near boundaries. However, it has been shown that the stability of diffusion operators can be improved, as seen using the example of the Laplacian [23].

2.2.2. Conservative

For the conservative approach, we omit optimization problem (10) and use Voronoi cells

$$\Omega_i = \{ \mathbf{x} \in \Omega \mid \|\mathbf{x} - \mathbf{x}_i\| < \|\mathbf{x} - \mathbf{x}_j\| \text{ for each } \mathbf{x}_j \in \Omega_h \setminus \{ \mathbf{x}_i \} \} \quad (18)$$

instead. For an inner point $\mathbf{x}_i \in \Omega$, we use cell mean values [28] to compute the discrete differential operator

$$|\Omega_i| L_i u = \int_{\Omega_i} \nabla \cdot (\eta \nabla u) \, d\mathbf{x}.$$

Applying the divergence theorem and exploiting the composition of the boundary of Ω_i into faces Γ_{ij} leads on to

$$|\Omega_i| L_i u = \oint_{\partial \Omega_i} \eta \frac{\partial u}{\partial \mathbf{n}} \, dS = \sum_{j \in S_i} \oint_{\Gamma_{ij}} \eta \frac{\partial u}{\partial \mathbf{n}} \, dS.$$

This way, we can represent the diffusion operator in terms of fluxes over the surfaces of the Voronoi cells. Note that for points $\mathbf{x}_j \in B_i$ that are not a Voronoi neighbor of \mathbf{x}_i , we use $\Gamma_{ij} = \emptyset$. For each face, we apply Gaussian quadrature

$$\oint_{\Gamma_{ij}} \eta \frac{\partial u}{\partial \mathbf{n}} \, dS \approx |\Gamma_{ij}| \eta_{ij} \frac{u_j - u_i}{d_{ij}}$$

where $\eta_{ij} \approx \eta(\mathbf{x}_{ij})$ is an approximation of η at the midpoint of the line segment L_{ij} between \mathbf{x}_i and \mathbf{x}_j and $d_{ij} = \|\mathbf{x}_j - \mathbf{x}_i\|$ is its length. Note that if the line segment L_{ij} and the surface Γ_{ij} intersect, then they intersect at exactly $\mathbf{x}_{ij} = \frac{\mathbf{x}_i + \mathbf{x}_j}{2}$.

Finally, the coefficients γ_{ij} for the discrete diffusion operator read

$$\gamma_{ij} = \frac{|\Gamma_{ij}| \eta_{ij}}{|\Omega_i| d_{ij}} \quad (19a)$$

where $i \neq j$ and for the diagonal entries

$$\gamma_{ii} = - \sum_{\substack{j \in \mathcal{S}_i \\ j \neq i}} \frac{|\Gamma_{ij}| \eta_{ij}}{|\Omega_i| d_{ij}}. \quad (19b)$$

These coefficients trivially fulfill diagonal dominance and the sign restriction $\gamma_{ii} < 0$ such that they automatically lead to diagonally dominant rows and thus fulfill the discrete maximum principle (14).

In the case of meshfree GFDM, we have a fixed distribution of points $\mathbf{x}_i \in \Omega$ based on which we can calculate the Voronoi cells. Except for few requirements presented by Seifarth [29], there are no restrictions on the point cloud or the resulting Voronoi cells. In contrast, mesh-based methods, such as the finite element method or the finite volume method have heavy restrictions that the mesh has to adhere to [30]. Furthermore, the Voronoi cells used here are constructed locally from the neighborhoods B_i and can thus easily be used for moving point clouds as well.

Calculation of η_{ij} . There are many ways to approximate η at the interface Γ_{ij} . One possibility is to use the values of η at the adjacent points and to compute the arithmetic mean

$$\eta_{ij} = \frac{\eta_i + \eta_j}{2}.$$

However, better results have been observed using the harmonic mean

$$\eta_{ij} = \frac{2}{\frac{1}{\eta_i} + \frac{1}{\eta_j}}.$$

Other approximation methods can be used, such as computing a discrete approximation operator with optimization problem (10) that discretizes the identity mapping

$$I_i u = u(\mathbf{x}_i).$$

This operator can be used to approximate function values at new points where the values were previously unknown. But for functions with large discontinuities this can lead to oscillations and even negative reconstructions $\eta_{ij} < 0$.

Conservative Neumann Boundary Condition. If we apply the cell mean value idea to boundary cells Ω_i that are associated to Neumann boundary points $\mathbf{x}_i \in \partial\Omega_N$ we obtain with similar calculations

$$\int_{\Omega_i} \nabla \cdot (\eta \nabla u) \, dS = \oint_{\Gamma_i} \eta \frac{\partial u}{\partial \mathbf{n}} \, dS + \sum_{j \in \mathcal{S}_i} \oint_{\Gamma_{ij}} \eta \frac{\partial u}{\partial \mathbf{n}} \, dS$$

where $\Gamma_i \subset \partial\Omega$ is a piece of the domain boundary associated to the boundary point \mathbf{x}_i . Using equations (1) and (2b) finally leads to

$$- \int_{\Omega_i} f \, d\mathbf{x} - \oint_{\Gamma_i} \eta g_N \, dS = \sum_{j \in \mathcal{S}_i} \oint_{\Gamma_{ij}} \eta \frac{\partial u}{\partial \mathbf{n}} \, dS.$$

Dividing by $|\Omega_i|$ and using the coefficients in equation (19), we find

$$- f_i - \frac{|\Gamma_i|}{|\Omega_i|} \eta_i g_N(\mathbf{x}_i) = \sum_{j \in \mathcal{S}_i} \gamma_{ij} u_j. \quad (20)$$

Discrete Divergence Theorem. The coefficients as in equations (19) and (20) satisfy the discrete divergence theorem

$$\int_{\Omega} \nabla \cdot (\eta \nabla u) \, d\mathbf{x} = \oint_{\partial\Omega} \eta \frac{\partial u}{\partial \mathbf{n}} \, dS.$$

For the divergence theorem to hold, we need to enforce the column sum condition

$$\sum_{i=1}^N |\Omega_i| \gamma_{ij} = 0 \quad (21)$$

for interior points $\mathbf{x}_j \in \Omega$ [23]. The cell-based approach automatically satisfies (21). However, if we tried to enforce (21) in the row-based discrete operator calculation from section 2.2.1, it is impossible to also set column-based properties without computing differential operators globally. This could lead to solving one huge optimization problem instead of solving many small optimization problems of the form of (10).

2.2.3. Hybrid

The computations of the Voronoi cells (18), even when done locally, can be costly and may be not be necessary at all points. If the diffusion coefficient η is smooth in a certain region, it is sufficient to use the classical approach from section 2.2.1 to obtain satisfactory results. Only in those regions, where the diffusivity has a discontinuity, we should switch to the conservative formulation from section 2.2.2. Thus, we need to identify regions where the classical approach fails. This can be achieved by checking the coefficients γ_{ij} that are obtained from the classical formulation. This way, we can define the diagonal dominance error

$$\sigma_i = \max \left(\sum_{\substack{j \in \mathcal{S}_i \\ j \neq i}} \frac{|\gamma_{ij}|}{|\gamma_{ii}|} - 1, \gamma_{ii}, 0 \right). \quad (22)$$

If $\sigma_i > 0$, we switch the approximation scheme to the conservative formulation. This leads to a hybrid numerical method that preserves the discrete maximum principle (14).

Better results can be achieved by using the conservative formulation not only for those points where $\sigma_i > 0$ but also for each neighboring point $j \in S_i$. However, this only results in a conservative scheme when we have symmetric neighborhoods which imposes a symmetry condition on the distance function in equation (5). Note that condition (22) checks only the diagonal dominance of a row. It can thus be triggered not only by high jumps in the diffusivity but also by local irregularities in the point cloud.

Other jump identification techniques exist where the function is directly screened for discontinuities, see for example [31, 32]. However, in their current formulation global properties of the examined function are used and thus these methods only work for one jump or multiple jumps with similar magnitudes.

3. Numerical Results

In the preceding sections, we have described numerical methods for approximating the diffusion operator. With that we have introduced a number of different parameters for computing the discrete differential operator. Parameters that are of special interest include

- number of smoothing cycles of the diffusivity
- scaling of the diffusion coefficient

for the strong form method. Furthermore, for the hybrid method

- extension of conservative method to the neighbors
- conservative Neumann boundaries.

Various parameter settings have been tested with select test cases that resemble varying difficulties of Poisson's equation. On the rectangle $\Omega = [-1, 1] \times [-1, 1]$ two different types of point clouds, uniform and irregular point clouds, have been used with increasing refinement levels $h = \frac{2 \times 10^{-1}}{2^k}$ for $k = 0, \dots, 5$. A comparison of the different point cloud types with similar refinements can be seen in figure 2. With this, we wanted to test if and to what extent an irregular point cloud influences the numerical results. Experiments have shown that by comparing numerical results from the different point cloud types, a small difference in the error could be observed, however the convergence behavior is comparable. In the following we will only show results from irregular point clouds as seen in figure 2b and specifically state where a uniform point cloud was used. Since the point clouds are generated independent of the diffusivity, we will show that our method works well on point clouds that do not conform to the interface.

To simplify notation, let us decompose the boundary of Ω into

$$\partial\Omega = \partial\Omega_L \cup \partial\Omega_R \cup \partial\Omega_T \cup \partial\Omega_B$$

into the left, right, top and bottom part respectively.

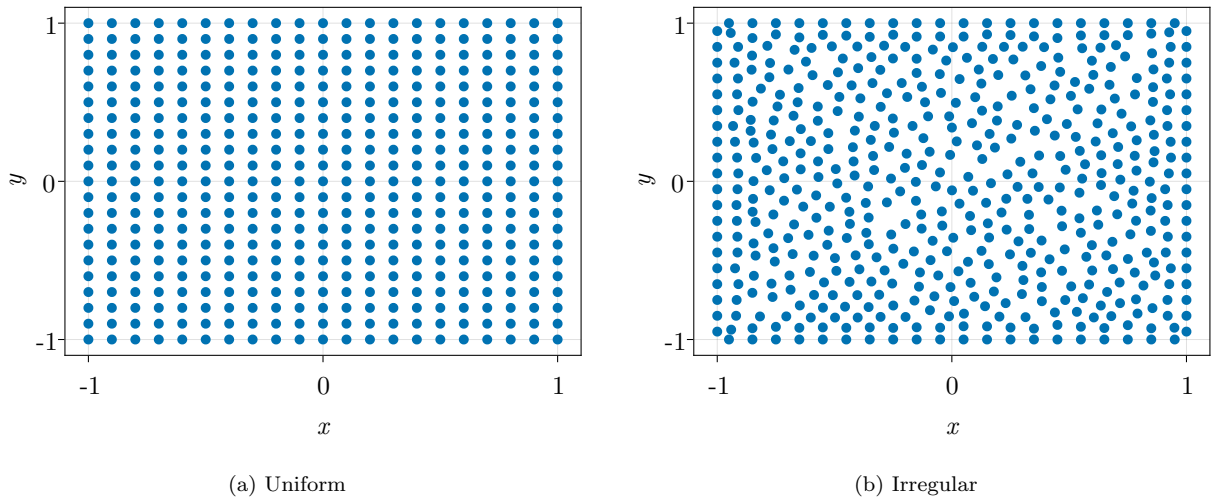


Figure 2: Comparison of point cloud types

3.1. Two Strip Problem

For the two strip problem, we solve the homogeneous Poisson's equation and define the diffusivity as a piecewise constant function

$$\eta(x, y) = \begin{cases} \eta_L, & x < 0, \\ \eta_R, & x > 0 \end{cases}$$

where $\eta_L, \eta_R > 0$. Additional Dirichlet and Neumann boundary conditions have been set

$$\begin{aligned} u|_{\partial\Omega_L} &= 2 \\ u|_{\partial\Omega_R} &= 1 \\ \frac{\partial u}{\partial \mathbf{n}} \Big|_{\partial\Omega_T} &= 0 \\ \frac{\partial u}{\partial \mathbf{n}} \Big|_{\partial\Omega_B} &= 0 \end{aligned}$$

that lead to an analytical solution that is monotonously decreasing and piecewise linear in x -direction and constant in y -direction. A two strip problem can be uniquely characterized either by the values η_L and η_R or by the jump

$$\delta\eta = \frac{\eta_R}{\eta_L}.$$

The solution profile of the analytical solution can be seen in figure 3 for a jump of $\delta\eta = 1 \times 10^8$. We note here that existing literature only considers jumps of up to 3 orders of magnitude, even for domain decomposition methods. For this test problem, we want to discuss if smoothing and the logarithmic scaling of the diffusion coefficient leads to better

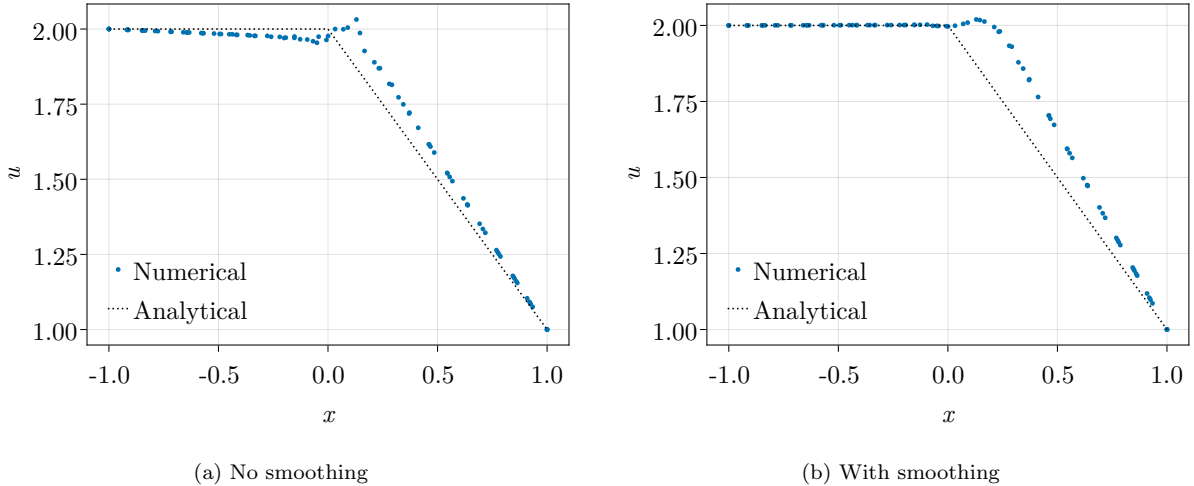
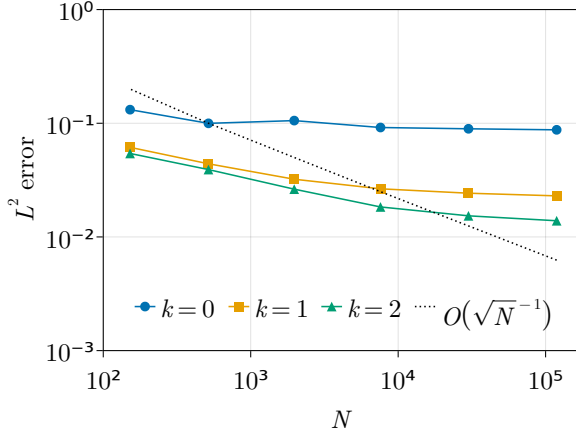


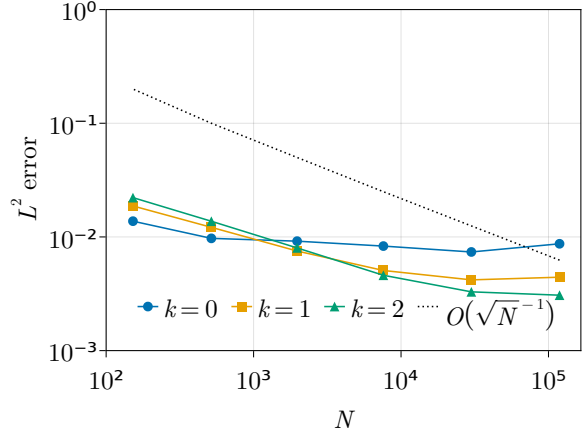
Figure 3: Solution profile at $y \in (-0.2, 0.2)$ to the two strip test case with a jump of $\delta\eta = 1 \times 10^8$.

results. We have produced results with zero, one and two smoothing cycles. Figure 4 shows that the classical method without smoothing or scaling does not show any convergence. If we apply scaling alone, we can observe that the method starts to converge for point clouds with a small point density but with an increasing number of points, the error stagnates. If we smooth the function, numerous effects can be seen. First, the method shows first order convergence even without a scaling of the diffusivity. A reason for that is that by smoothing the function, the discrete gradient operates better on the diffusivity since it does not have a discontinuity. Secondly, if we additionally scale the diffusivity, the error is reduced for all methods. Another important conclusion that we can draw from these results is that increasing the number of smoothing cycles does not necessarily lead to better results as can be seen in figure 4d. This is due to increasing distortion of our problem with an increasing number of smoothing cycles. We can also observe that for some point clouds, the non-smoothed diffusivity leads to better results than the smoothed diffusivity, as can be seen in figures 4b and 4d. In figure 5 we computed the L^2 errors depending on the jump on a fixed point cloud with the highest refinement. It shows that the methods with a smoothed diffusivity are less susceptible for high jump magnitudes. However, it also shows that the error can be reduced by a factor of 6 to 10 for the non-smoothed version and by a factor of approximately 4 for the smoothed versions by adding logarithmic scaling.

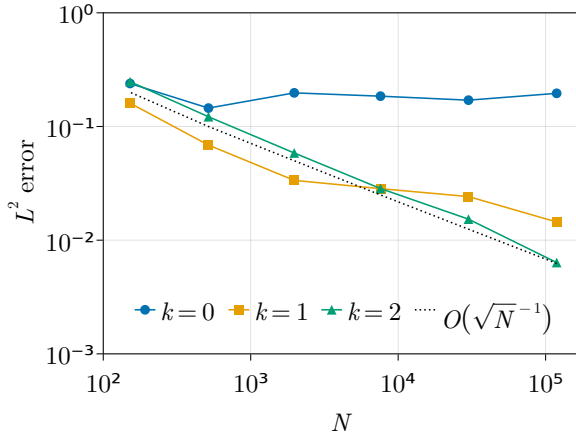
With this information, we can establish the “best” strong form method considered as a method that includes the scaling of the diffusivity and, depending on the magnitude of the jump, some smoothing of it. From the results, it can be doubted if the smoothing improves the numerical solution. But it can be seen that it stabilizes the convergence. Additionally, the non-scaled version tends to have overshoots in the region of the interface and the smoothing causes the overshoot to smear out but not disappear, see figures 3a and 3b. This behavior is characteristic for strong form methods and can already be seen in the smoothing method presented by Li and Ito [33]. In the following, we will choose the strong form method with a scaled diffusivity and 2 smoothing cycles for comparisons.



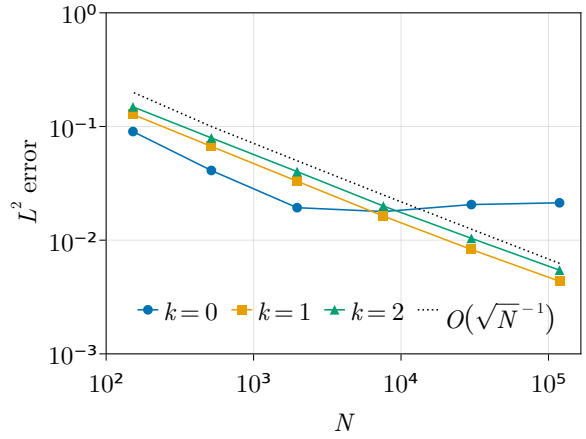
(a) No scaling, $\delta\eta = 1 \times 10^1$



(b) Logarithmic scaling, $\delta\eta = 1 \times 10^1$



(c) No scaling, $\delta\eta = 1 \times 10^{10}$



(d) Logarithmic scaling, $\delta\eta = 1 \times 10^{10}$

Figure 4: Convergence plots of the classical strong form method for the two strip test case with and without logarithmic scaling with different jumps $\delta\eta$ and number of smoothing cycles k .

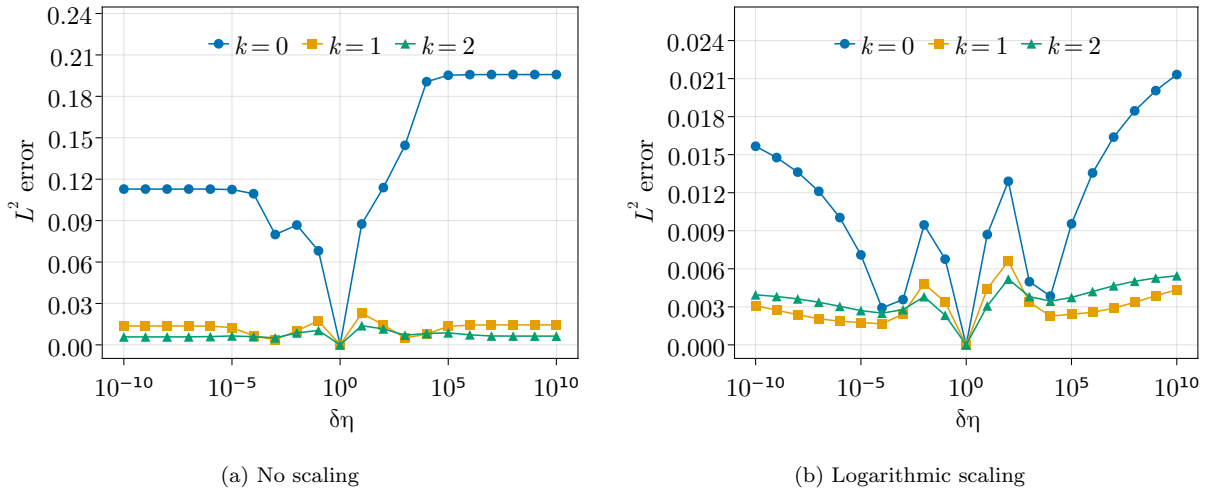


Figure 5: L^2 errors for the two strip test case depending on the jump $\delta\eta$.

Next, we want to compare this strong form method to the hybrid method. We distinguish between the hybrid method where we switch to the conservative formulation only for those points where diagonal dominance could not be achieved by the strong form method, and the hybrid method where we switch the formulation for the entire neighborhood of such points. For now, let us only consider the method where the formulation switches for those points where no diagonal dominance could be achieved by the strong form method. The other options will be introduced in the following examples. Figure 6 illustrates the difference between the strong form and the hybrid method for a small jump of only $\delta\eta = 1 \times 10^1$ (figure 6a) and a high jump of $\delta\eta = 1 \times 10^{10}$ (figure 6b). In figure 6a we can clearly see that the hybrid method does not show any convergence. In fact, the method is providing almost identical results as the scaled strong form method without smoothing as in figure 4b. This shows that for this small jump, the classical formulation already has a diagonally dominant row and only few points that have a distorted neighborhood will use the conservative scheme. In fact, we obtain the same results if we compare both methods on uniform point clouds as seen in figure 2a. However, if we increase the magnitude of the jump, the error of the hybrid method reduces in comparison to the strong form method, see figure 6b. This shows that diagonal dominance depends on both, the quality of the point cloud and sufficient regularity of the diffusion.

3.2. Curved Interface

We now consider a test case with a more complex interface. This test case is inspired by Davydov and Safarpour [5] with a modification to allow different jump magnitudes. The interface is given as

$$\Gamma = \{ (x, y) \in \Omega \mid y = 2x^3 \}$$

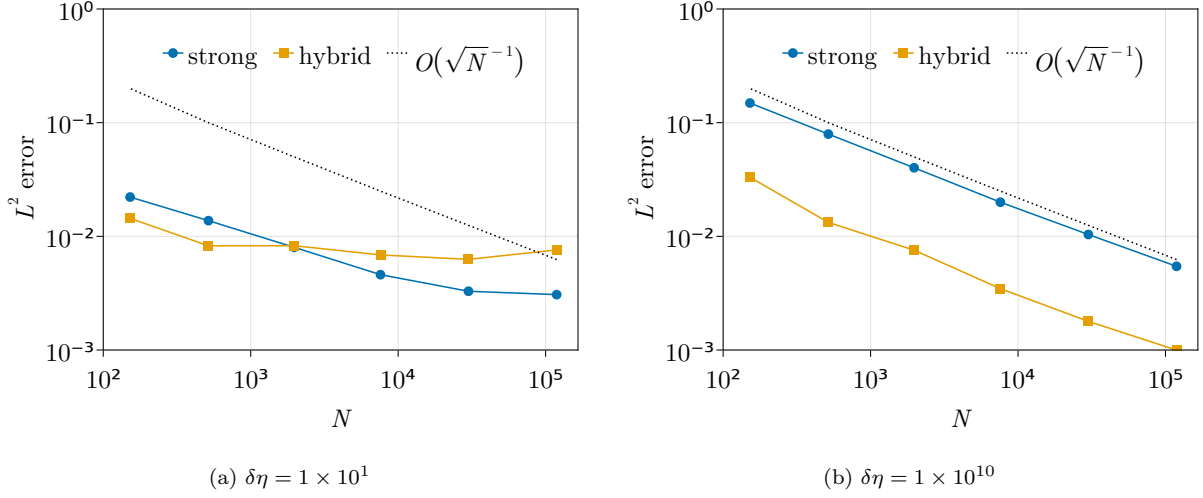


Figure 6: L^2 errors of strong form method and hybrid method for the two strip test case with different jump magnitudes.

which leads to the diffusivity

$$\eta(x, y) = \begin{cases} \eta_L, & y > 2x^3, \\ \eta_R, & y < 2x^3. \end{cases}$$

The source term is defined as

$$f(x, y) = -120x^4 + 24x(y - 15) - 2$$

leading to an inhomogeneous Poisson's equation with Dirichlet boundary conditions on the complete boundary such that the analytical solution

$$u(x, y) = \frac{(y - 2x^3)^2 - 30(y - 2x^3)}{\eta(x, y)}$$

is obtained. We have computed results for different jumps

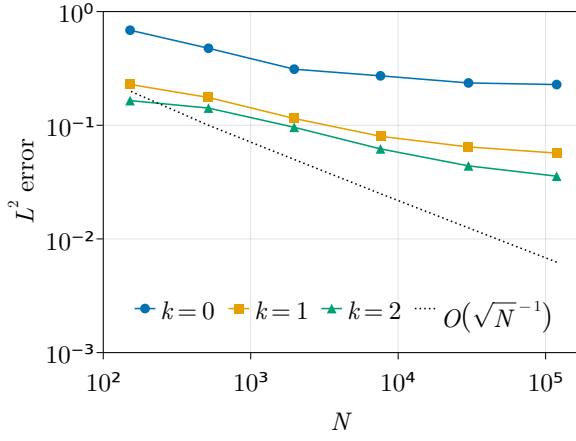
$$\delta\eta = \frac{\eta_R}{\eta_L}.$$

Unlike the previous test case, the solution in this test case depends not only on the jump $\delta\eta$ but also on the values. In order to avoid high gradients for u , we have used

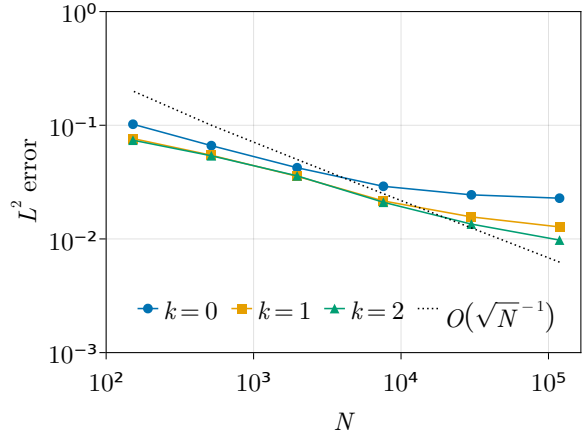
$$\eta_R = 10^m$$

for a fixed $\eta_L = 1$ and

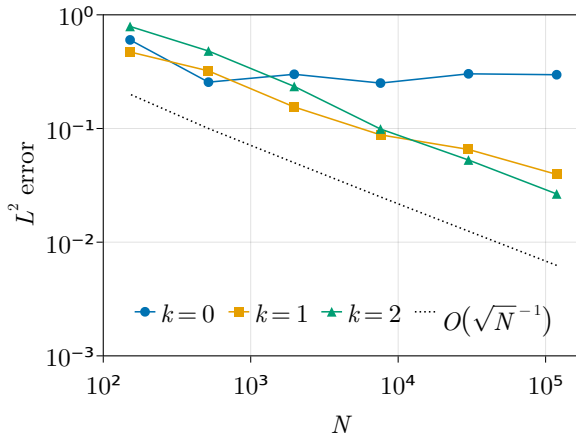
$$\eta_L = 10^m$$



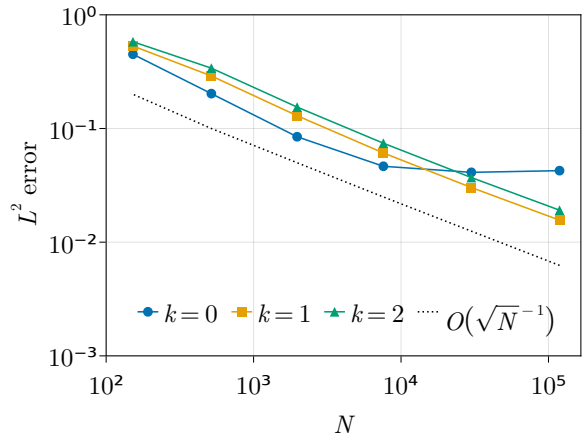
(a) No scaling, $\delta\eta = 1 \times 10^1$



(b) Logarithmic scaling, $\delta\eta = 1 \times 10^1$

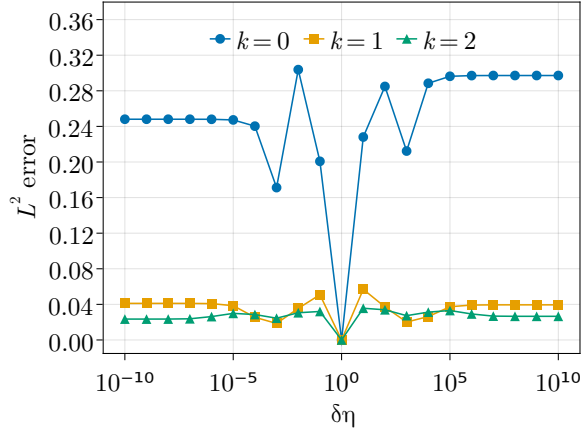


(c) No scaling, $\delta\eta = 1 \times 10^{10}$

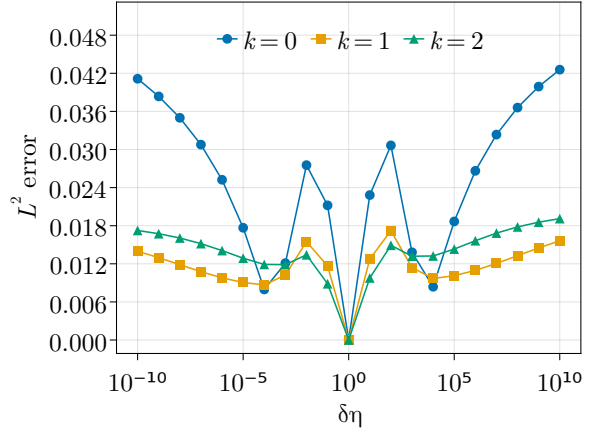


(d) Logarithmic scaling, $\delta\eta = 1 \times 10^{10}$

Figure 7: Convergence plots of the classical strong form method for the curved interface test case with and without logarithmic scaling with different jumps $\delta\eta$ and number of smoothing cycles k .

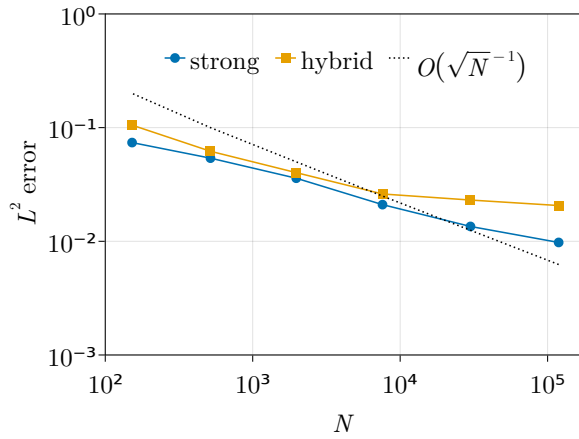


(a) No scaling

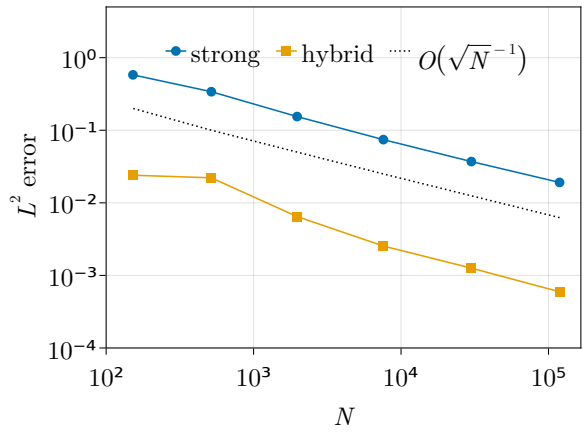


(b) Logarithmic scaling

Figure 8: L^2 errors for the curved interface test case depending on the jump $\delta\eta$.



(a) $\delta\eta = 1 \times 10^1$



(b) $\delta\eta = 1 \times 10^{10}$

Figure 9: L^2 errors of strong form method and hybrid method for the curved interface test case with different jump magnitudes.

for a fixed $\eta_R = 1$ where $m = 0, \dots, 10$.

Generally, figures 7 and 8 qualitatively show similar results to the two strip problem for the strong form method, however higher errors can be observed in comparison. Similarly, higher errors can be observed in the comparison of the hybrid and the strong form method in figure 9 in comparison to the two strip problem. The general trends of the impact of scaling and smoothing observed here are the same as for the two strip test case, which leads to the conclusion that the curvature of the interface has no significant impact on the numerical methods. In summary, we draw similar conclusions as for the two strip test case.

3.3. Interior Interface

Unlike the above two test cases, here we consider a diffusivity function that has a discontinuity that does not intersect a domain boundary. For this test problem we define the function

$$\phi(x, y) = \cos(\pi x/2) \cos(\pi y/2)$$

and for the inhomogeneous Poisson's equation, we set the right-hand side

$$f(x, y) = -\Delta\phi(x, y) = \frac{\pi^2}{2}\phi(x, y).$$

Additionally, the Dirichlet boundary condition

$$u|_{\partial\Omega} = 0$$

is set and given a height $H \in (0, 1)$, we define the diffusivity

$$\eta(x, y) = \begin{cases} \eta_{\text{out}}, & \phi(x, y) < H, \\ \eta_{\text{in}}, & \phi(x, y) > H \end{cases}$$

with $\eta_{\text{out}} = 1$ and $\eta_{\text{in}} = 10^k$ for $k = 0, \dots, 10$. That way, the function

$$u = \frac{\phi - H}{\eta} + H$$

solves the inhomogeneous Poisson's equation with jump conditions (4). In our case $H = \frac{3}{4}$ is set which leads to a fully interior interface $\Gamma \subset \Omega$ that separates the domain into Ω_{in} and Ω_{out} . This test problem has the additional challenge that the interior domain Ω_{in} is entirely contained within Ω and thus has no Dirichlet boundary. This means that the jump conditions have to be propagated across the interface by the discrete diffusion operator. For this test case we want to look at the option of extending the hybrid method to the neighborhoods of such points where diagonal dominance could not be achieved by the strong form method. In previous tests we have seen that for small magnitudes, the jumps are not identified by the diagonal dominance criterion. Hence, we will focus on large jumps of several orders of magnitude for this test case.

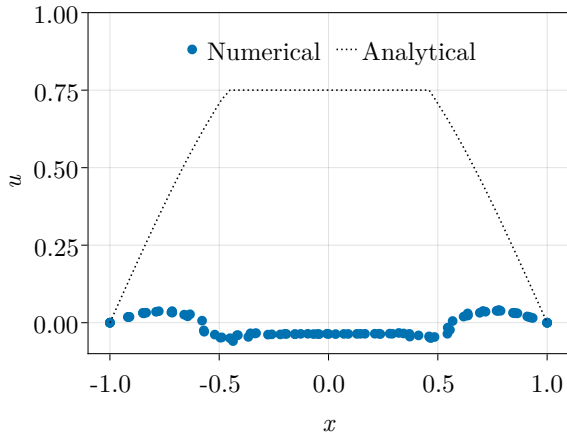
We will distinguish between three methods. The strong form method is based on the monomial reproducibility enforced with optimization problem (10). The positivity preserving hybrid method is the hybrid approach where we switch to the conservative formulation only for points where diagonal dominance could not be achieved by the strong form method. This results in an M-matrix in the linear system (12) hence the method is positivity preserving in the sense of (14). Finally, the conservative hybrid method switches to the conservative formulation in the entire neighborhoods of such points, which leads to it begin locally conservative additionally to being positivity preserving since it fulfills the row sum condition (21).

Note that since $f \geq 0$ on Ω , according to the maximum principle (13) we expect $u \geq 0$. In experiments, it could be observed that the strong form method could not satisfy this in all circumstances. Figure 10a shows that the strong form method without smoothing fails to provide positive solutions and with smoothing, we can observe the characteristic smeared-out overshoots as could be seen for the two strip problem, see figure 10b. Switching to the positivity preserving scheme, we have a guaranteed positivity of the numerical solution. However, the obtained solution is not necessarily correct with respect to the jump conditions (4), see figure 10c. This is due to points \mathbf{x}_i with, for example, $\eta_i = \eta_{\text{in}}$ that have a point $j \in S_i$ in its neighborhood with $\eta_j = \eta_{\text{out}}$ where a diagonally dominant strong form operator could be established. Thus, flux conservation is not necessarily satisfied for these points and we need to extend the conservative scheme to these points as well. This results in a good alignment of the numerical and the analytical solution in figure 10d. This behavior can be confirmed for different jump magnitudes in figure 11 where the positivity preserving method fails to provide first order convergence. However, the conservative method has first order convergence and this shows that the strong form scheme produces diagonally dominant discrete operators for some points that have their neighborhoods across the interface, as described earlier. Additionally, the conservative method shows to be insensitive to the jump magnitude as can be seen in figure 12. In summary, the conservative scheme shows best results for high jumps and thus should be the preferred method.

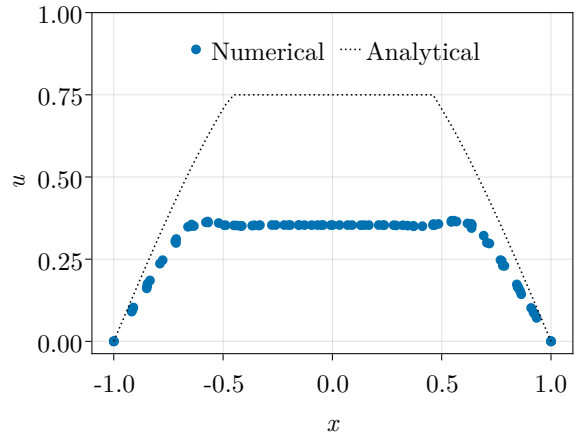
3.4. Three Strip Problem

Similarly to the two strip test case, we define the diffusivity with three positive values η_L , η_M and η_R

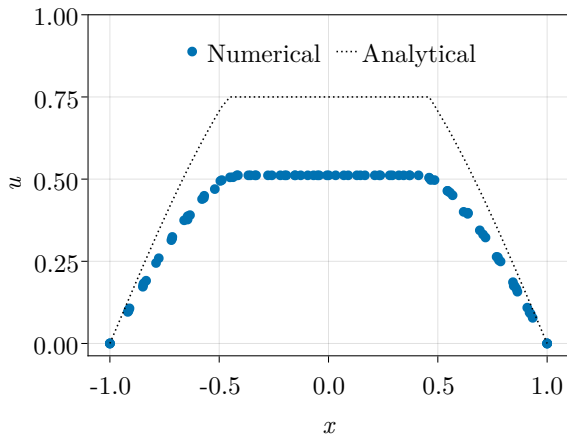
$$\eta(x, y) = \begin{cases} \eta_L, & x < -\frac{1}{3}, \\ \eta_M, & -\frac{1}{3} < x < \frac{1}{3}, \\ \eta_R, & x > \frac{1}{3} \end{cases}$$



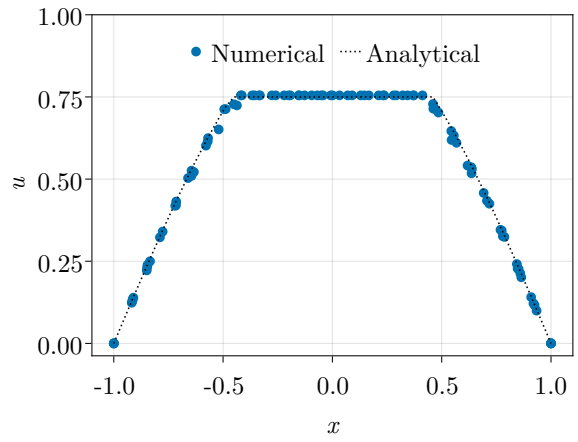
(a) Strong form method without smoothing



(b) Strong form method with smoothing

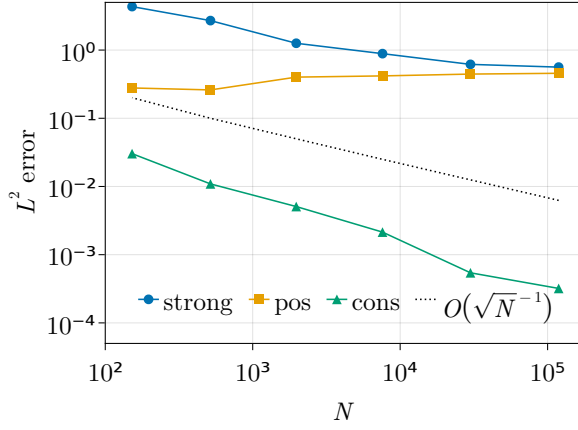


(c) Positivity preserving hybrid method

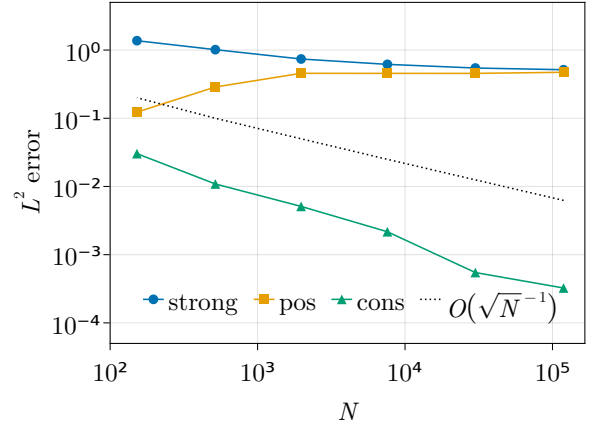


(d) Conservative hybrid method

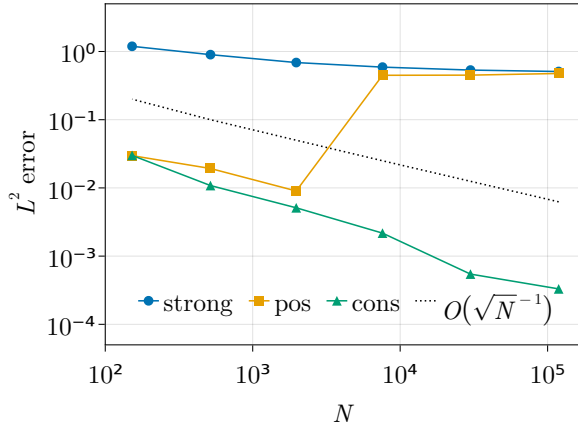
Figure 10: Solution profile at $y \approx 0$ to the interior interface test case with a jump of $\delta\eta = 1 \times 10^6$.



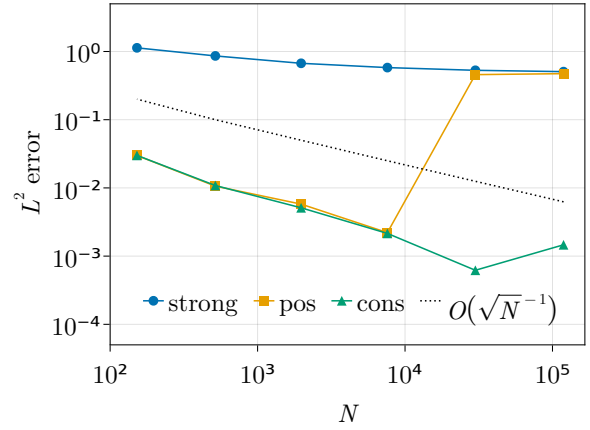
(a) $\delta\eta = 1 \times 10^4$



(b) $\delta\eta = 1 \times 10^6$



(c) $\delta\eta = 1 \times 10^8$



(d) $\delta\eta = 1 \times 10^{10}$

Figure 11: Convergence plots of the classical strong form method, the positivity-preserving method (pos) and the conservative method (cons) for the interior interface test case with different jumps $\delta\eta$.

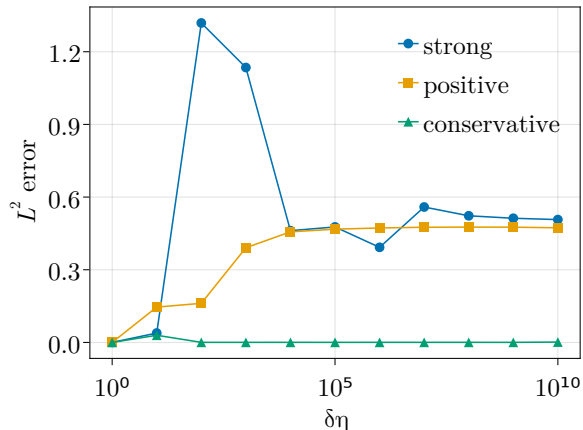


Figure 12: L^2 errors for the interior interface test case depending on the jump $\delta\eta$.

that leads to three equally sized strips

$$\begin{aligned}\Omega_L &= \left\{ (x, y) \in \Omega \mid x < -\frac{1}{3} \right\}, \\ \Omega_M &= \left\{ (x, y) \in \Omega \mid -\frac{1}{3} < x < \frac{1}{3} \right\}, \\ \Omega_R &= \left\{ (x, y) \in \Omega \mid x > \frac{1}{3} \right\}.\end{aligned}$$

Dirichlet and Neumann boundary conditions are set exactly as for the two strip test case such that the analytical solution is again monotonously decreasing and piecewise linear in x -direction. A three strip problem can be characterized by the two jumps at the interfaces

$$\begin{aligned}\delta\eta_L &= \frac{\eta_M}{\eta_L}, \\ \delta\eta_R &= \frac{\eta_R}{\eta_M}\end{aligned}$$

and with $\eta_L = 1$ we have

$$\begin{aligned}\eta_M &= \delta\eta_L, \\ \eta_R &= \delta\eta_L \delta\eta_R.\end{aligned}$$

In this test case, we added additional complexity to the problem by essentially partitioning the domain into the three strips where Ω_M is not directly connected to a Dirichlet boundary. The only boundary conditions that appear for this subdomain are Neumann boundary conditions and this introduces additional challenges to the numerical scheme in use.

1. We need the numerical scheme to propagate the jump conditions (4) from the surrounding domains Ω_L and Ω_R correctly.

2. Neumann boundary conditions near the interface need to use the correct information across interface boundaries.

We know from the previous experiment with the interior interface test case that the jump propagation across interfaces works best with the conservative method. However, problems arise from the Neumann boundary where false jump conditions are propagated. For this experiment, we want to examine if the conservative Neumann boundary conditions can be used to improve numerical results. We use conservative Neumann boundary conditions in the neighborhood of points where a switch to the conservative formulation is realized. We have observed that the standard hybrid method did not converge for this test case as can be seen in figure 13. A view on figure 14a shows that the analytical solution is not reached. A reason for that is the lack of flux conservation [18]. For a numerical solution u_h let us define the error in flux by

$$\delta q = \eta \partial_x (u - u_h).$$

Since we are looking for a solution of the homogeneous Poisson's equation, the function δq has to be piecewise constant and continuous which leads to it being constant throughout the domain. A view on figure 15a shows that δq for the numerical solution without conservative Neumann boundary conditions is not constant. This observation can be made especially at the boundaries $\partial\Omega_T$ and $\partial\Omega_B$ which lead to the assumption that flux conservation has to be met at the boundary as well. Finally, switching to conservative Neumann boundary conditions, we can see in figures 14b and 15b that the analytical solution matches the numerical solution visually and δq has less oscillations. Figure 13 confirms that the method is first order accurate with conservative Neumann boundary conditions.

To better illustrate δq in figure 15, a domain decomposition based on η was executed to be able to calculate the gradient $\nabla u|_{\Omega_*}$ on each subdomain Ω_L , Ω_M and Ω_R without the influence of the neighboring subdomains. The numerical results were computed without the use of a domain decomposition. Note that the outliers on figure 15b are due to the distortedness of the point cloud and the circumstance that we calculate the gradient near the interface which serves as a boundary to the subdomains. If we compute δq on a uniform point cloud, we obtain figure 16 and thus

$$\delta q_i = c + \varepsilon_i$$

for a numerically computed constant $c \approx -1.834 \times 10^{-2}$ and an error

$$\max_{i=1,\dots,N} |\varepsilon_i| = O(1 \times 10^{-8})$$

which is negligible.

4. Discussion

We have seen many results in the previous section. This section aims to provide a summary of the numerical results and consequences that we can draw from them.

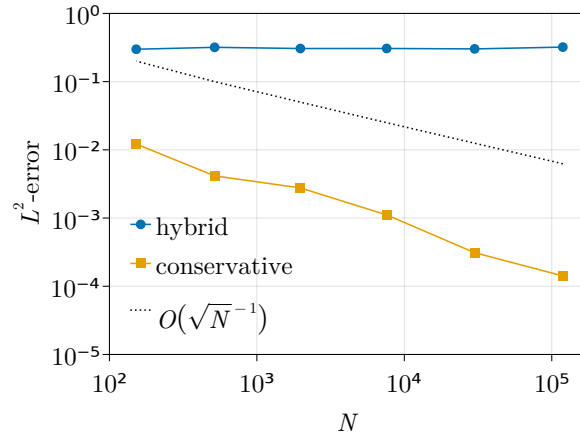
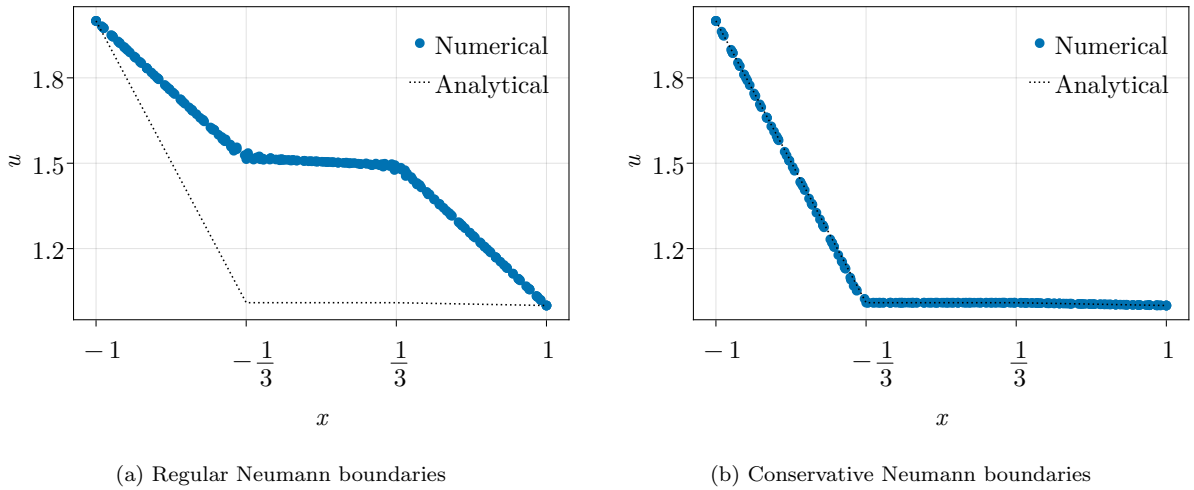


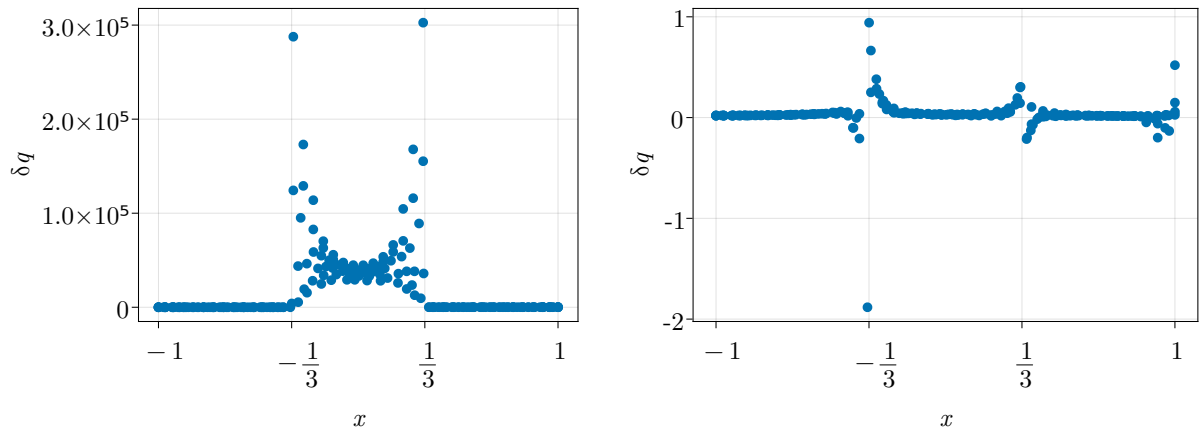
Figure 13: L^2 errors for the three strip test case of hybrid method with and without conservative Neumann boundary conditions for a jump $\delta\eta_L = 1 \times 10^6$ and $\delta\eta_R = 1 \times 10^{-4}$.



(a) Regular Neumann boundaries

(b) Conservative Neumann boundaries

Figure 14: Solution profiles comparison at $y \approx 0$ for the three strip test case of hybrid method with and without conservative Neumann boundary conditions for a jump $\delta\eta_L = 1 \times 10^6$ and $\delta\eta_R = 1 \times 10^{-4}$.



(a) Regular Neumann boundaries

(b) Conservative Neumann boundaries

Figure 15: Profiles of $\delta q = \eta \partial_x(u - u_h)$ at $y \approx 0$ for the three strip test case of hybrid method with and without conservative Neumann boundary conditions for a jump $\delta\eta_L = 1 \times 10^6$ and $\delta\eta_R = 1 \times 10^{-4}$ on an irregular point cloud.

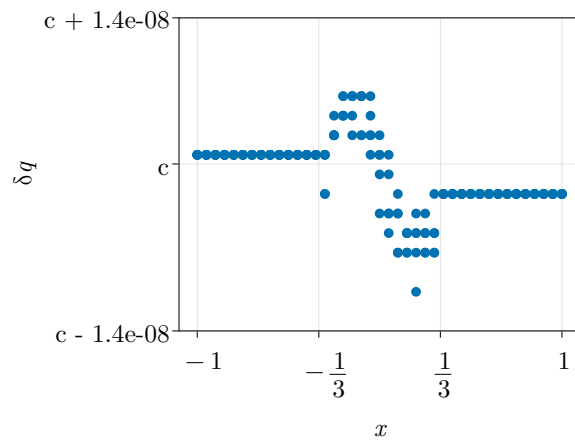


Figure 16: Profile of $\delta q = \eta \partial_x(u - u_h)$ at $y \approx 0$ for the three strip test case of hybrid method with conservative Neumann boundary conditions for a jump $\delta\eta_L = 1 \times 10^6$ and $\delta\eta_R = 1 \times 10^{-4}$ on a uniform point cloud.

Our first observation was that artificial smoothing could help stabilize the convergence behavior of the strong form method for very simple test cases. However, we have also seen other test cases where the strong form method failed to provide accurate solutions, regardless of whether we smooth or not. Thus, the first consequence is that artificial smoothing should be avoided because it distorts the data from the mathematical model.

For the hybrid method, we can conclude that it produces good results and provides first order convergence in its current form. One limitation is the need of a Voronoi cell that has to be computed. Finally, we saw that placing conservative Neumann boundary conditions is necessary for the three strip test case.

The presented switch between the strong form and weak form guarantees positivity of the numerical solution and the fulfillment of the discrete divergence theorem locally. One major drawback of the presented switch is its dependence on the jump magnitude and the level of the distortedness of the point cloud and not the mere existence of a jump in the diffusion coefficients.

5. Conclusion

In this paper, we presented two approaches of discretizing the diffusion operator and a new way of combining these approaches in a locally conservative and positivity preserving method. Our approach combines the cell mean value-based conservative formulation and the strong form GFDM into a new method. It puts the finite volume method idea inside the context of GFDM and uses its advantages without sacrificing the advantages that GFDM offers, namely the flexibility of the point cloud. This is a major benefit with respect to time-dependent problems in a Lagrangian formulation with a moving point cloud, which will be an extension of the present work.

We performed an in-depth study on different test cases with different parameter settings of the methods. We have considered jumps up to ten orders of magnitude whereas existing methods were limited to three orders of magnitude. Our numerical results show that the classical GFDM approach fails for high jump magnitudes and that conservation is necessary. Finally, we have seen that it can be necessary to incorporate conservative Neumann boundary conditions to guarantee the conservation property of the entire numerical scheme. Since our computations were carried out on non-conforming point clouds, we could show that the presented method does not depend on aligning the point cloud to the interface.

The discretization of the diffusion operator is subject to ongoing research and as such open questions remain. For the diffusion operator, one possibility is to use shapeless volumes and higher order approximations. Additionally, the jump identification technique can be extended for it to be able to identify lower jumps. While this is not needed for our applications, it might be necessary for others.

6. Acknowledgements

Pratik Suchde would like to acknowledge support from the European Union’s Horizon 2020 research and innovation programme under the Marie Skłodowska-Curie Actions grant agreement No. 892761 “SURFING”.

References

- [1] L. Gavete, F. Ureña Prieto, J. J. Benito, Á. García, M. Ureña, E. Saletе, Solving second order non-linear elliptic partial differential equations using generalized finite difference method, *Journal of computational and applied mathematics* 318 (2017) 378–387. doi:10.1016/j.cam.2016.07.025.
- [2] T. J. Liszka, J. Orkisz, The finite difference method at arbitrary irregular grids and its application in applied mechanics, *Computers & structures* 11 (1980) 83–95. doi:10.1016/0045-7949(80)90149-2.
- [3] T. Belytschko, Y. Krongauz, D. Organ, M. Fleming, P. Krysl, Meshless methods: An overview and recent developments, *Computer methods in applied mechanics and engineering* 139 (1996) 3–47. doi:10.1016/s0045-7825(96)01078-x.
- [4] P. Suchde, H. Kraus, B. Bock-Marbach, J. Kuhnert, Meshfree one-fluid modelling of liquid-vapor phase transitions, preprint arXiv:2203.10383 (2022).
- [5] O. Davydov, M. Safarpour, A meshless finite difference method for elliptic interface problems based on pivoted qr decomposition, *Applied numerical mathematics: transactions of IMACS* 161 (2021) 489–509. doi:10.1016/j.apnum.2020.11.018.
- [6] M. Shao, L. Song, P.-W. Li, A generalized finite difference method for solving stokes interface problems, *Engineering analysis with boundary elements* 132 (2021) 50–64. doi:10.1016/j.enganabound.2021.07.002.
- [7] F. Gibou, L. Chen, D. Nguyen, S. Banerjee, A level set based sharp interface method for the multiphase incompressible navier–stokes equations with phase change, *Journal of computational physics* 222 (2007) 536–555. doi:10.1016/j.jcp.2006.07.035.
- [8] Y.-C. Yoon, J.-H. Song, Extended particle difference method for weak and strong discontinuity problems: part i. derivation of the extended particle derivative approximation for the representation of weak and strong discontinuities, *Computational mechanics* 53 (2014) 1087–1103. doi:10.1007/s00466-013-0950-8.
- [9] P. Suchde, J. Kuhnert, A meshfree generalized finite difference method for surface pdes, *Computers & mathematics with applications (Oxford, England: 1987)* 78 (2019) 2789–2805. doi:10.1016/j.camwa.2019.04.030.
- [10] T.-P. Fries, T. Belytschko, The extended/generalized finite element method: An overview of the method and its applications, *International journal for numerical methods in engineering* 84 (2010) 253–304. doi:10.1002/nme.2914.
- [11] K. Agathos, E. Chatzi, S. P. A. Bordas, Stable 3d extended finite elements with higher order enrichment for accurate non planar fracture, *Computer methods in applied mechanics and engineering* 306 (2016) 19–46. doi:10.1016/j.cma.2016.03.023.
- [12] S. P. A. Bordas, S. Natarajan, P. Kerfriden, C. E. Augarde, D. R. Mahapatra, T. Rabczuk, S. D. Pont, On the performance of strain smoothing for quadratic and enriched finite element approximations (xfem/gfem/pufem), *International journal for numerical methods in engineering* 86 (2011) 637–666. doi:10.1002/nme.3156.
- [13] E. O. Reséndiz-Flores, F. R. Saucedo-Zendejo, Numerical simulation of coupled fluid flow and heat transfer with phase change using the finite pointset method, *International journal of thermal sciences* 133 (2018) 13–21. doi:10.1016/j.ijthermalsci.2018.07.008.
- [14] F. R. Saucedo-Zendejo, E. O. Reséndiz-Flores, Transient heat transfer and solidification modelling in direct-chill casting using a generalized finite differences method, *Journal of Mining and Metallurgy Section B Metallurgy* 55 (2019) 47–54. doi:10.2298/jmmb180214005s.
- [15] N. Trask, M. Perego, P. Bochev, A high-order staggered meshless method for elliptic problems, *SIAM journal on scientific computing: a publication of the Society for Industrial and Applied Mathematics* 39 (2017) A479–A502. doi:10.1137/16m1055992.
- [16] J. Kuhnert, Meshfree numerical schemes for time dependent problems in fluid and continuum mechanics, 2014, pp. 119–136.
- [17] J. Kuhnert, An upwind finite pointset method (FPM) for compressible Euler and Navier-stokes equations, Springer Berlin Heidelberg, 2003.

- [18] P. Suchde, J. Kuhnert, S. Schröder, A. Klar, A flux conserving meshfree method for conservation laws, *International journal for numerical methods in engineering* 112 (2017) 238–256. doi:10.1002/nme.5511.
- [19] E. Kwan-yu Chiu, Q. Wang, R. Hu, A. Jameson, A conservative mesh-free scheme and generalized framework for conservation laws, *SIAM journal on scientific computing: a publication of the Society for Industrial and Applied Mathematics* 34 (2012) A2896–A2916. doi:10.1137/110842740.
- [20] M. Chipot, *Elliptic equations: An introductory course*, Springer, 2009.
- [21] S. Milewski, Meshless finite difference method with higher order approximation—applications in mechanics, *Archives of Computational Methods in Engineering. State of the Art Reviews* 19 (2012) 1–49. doi:10.1007/s11831-012-9068-y.
- [22] S. Milewski, Combination of the meshless finite difference approach with the monte carlo random walk technique for solution of elliptic problems, *Computers & mathematics with applications* (Oxford, England: 1987) 76 (2018) 854–876. doi:10.1016/j.camwa.2018.05.025.
- [23] P. Suchde, *Conservation and accuracy in meshfree generalized finite difference methods*, Fraunhofer Verlag, 2018.
- [24] W. Qu, Y. Gu, Y. Zhang, C.-M. Fan, C. Zhang, A combined scheme of generalized finite difference method and krylov deferred correction technique for highly accurate solution of transient heat conduction problems, *International journal for numerical methods in engineering* 117 (2019) 63–83. doi:10.1002/nme.5948.
- [25] P.-W. Li, C.-M. Fan, Generalized finite difference method for two-dimensional shallow water equations, *Engineering analysis with boundary elements* 80 (2017) 58–71. doi:10.1016/j.enganabound.2017.03.012.
- [26] Z. Li, K. Ito, Maximum principle preserving schemes for interface problems with discontinuous coefficients, *SIAM journal on scientific computing: a publication of the Society for Industrial and Applied Mathematics* 23 (2001) 339–361. doi:10.1137/s1064827500370160.
- [27] B. Seibold, *M-Matrices in Meshless Finite Difference Methods*, Shaker Verlag, 2006.
- [28] R. Eymard, T. Gallouët, R. Herbin, *Finite Volume Methods*, volume 7 of *Handbook of Numerical Analysis*, Elsevier, 2000, pp. 713–1018. doi:10.1016/S1570-8659(00)07005-8.
- [29] T. Seifarth, *Numerische Algorithmen für gitterfreie Methoden zur Lösung von Transportproblemen*, Fraunhofer Verlag, 2018.
- [30] P. M. Knupp, Algebraic mesh quality metrics, *SIAM journal on scientific computing: a publication of the Society for Industrial and Applied Mathematics* 23 (2001) 193–218. doi:10.1137/s1064827500371499.
- [31] G. Allasia, R. Besenghi, R. Cavoretto, Adaptive detection and approximation of unknown surface discontinuities from scattered data, *Simulation modelling practice and theory* 17 (2009) 1059–1070. doi:10.1016/j.simpat.2009.03.007.
- [32] T. Gutzmer, A. Iske, Detection of discontinuities in scattered data approximation, *Numerical Algorithms* 16 (1997) 155–170. doi:10.1023/a:1019139130423.
- [33] Z. Li, K. Ito, *The immersed interface method: Numerical solutions of PDEs involving interfaces and irregular domains*, Society for Industrial and Applied Mathematics, 2006.